



A time-dependent non-Newtonian extension of a 1D blood flow model

A.R. Ghigo, P.-Y. Lagrée, J.-M. Fullana*

Sorbonne Université, CNRS and UPMC Université Paris 06, UMR 7190, Institut Jean Le Rond d'Alembert, 4 place Jussieu, Boîte 162, Paris 75005, France



ARTICLE INFO

Keywords:
Arterial network
1D model

ABSTRACT

Blood pulsatility, aneurysms, stenoses and general low shear stress hemodynamics enhance non-Newtonian blood effects which generate local changes in the space-time evolution of the blood pressure, flow rate and cross-sectional area of elastic vessels. Even though these local changes are known to cause global unexpected hemodynamical behaviors, all one-dimensional (1D) blood flow models are built under Newtonian fluid hypothesis.

In this work, we present a time-dependent non-Newtonian extension of a 1D blood flow model, able to describe local space-time variations of the viscous behavior of blood. The rheological model is based on a simplified Maxwell viscoelastic equation for the shear stress with structure dependent coefficients. We compare the numerical predictions of the 1D non-Newtonian model to experimental rheological data available in the literature. Specifically, we explore four well documented shear stress protocols and we show that the results predicted by the 1D non-Newtonian model in a single artery accurately compare, both qualitatively and quantitatively, to the steady and unsteady shear stresses measured experimentally. We then use the 1D non-Newtonian model to compute the flow in idealized healthy and pathological symmetric and asymmetric networks of increasing size. We show that aggregation occurs in such networks occurs, leading to non-Newtonian blood behaviors especially in the presence of pathologies.

This non-Newtonian extension of a 1D blood flow model will be useful in the future to improve our understanding of the large-scale hemodynamics in micro- and macro-circulation networks.

1. Introduction

In recent years, one-dimensional (1D) blood flow models have greatly helped clinicians understand the complex wave propagation dynamics occurring in the systemic circulation, which are a combination of forward waves traveling from the heart and backward waves reflected at arterial junctions and in the arterioles. Indeed, 1D blood flow models enable an efficient and accurate description of averaged blood flow features [1,2]. They are therefore particularly well-suited for the study of blood flow in large arterial networks [3] and are now being used as predictive tools for clinical studies [4–6]. In comparison, three-dimensional (3D) approaches are more accurate but more costly and time-consuming, especially in deformable elastic vessels. They are therefore restricted to small networks of only a few arteries [7–10] and depend on appropriate boundary conditions to reproduce physiological data [7,11–13].

These 1D blood flow models rely on a series of simplifying assumptions, among which is the hypothesis that blood is a Newtonian fluid. While mostly valid in high shear regions such as healthy large arteries (typically the shear rate $\dot{\gamma} \geq 10 \text{ s}^{-1}$), there are many portions of

the systemic circulation where low shear regimes are reached (typically the shear rate $\dot{\gamma} \leq 1 \text{ s}^{-1}$) as a consequence of the pulsatility of blood flow and of recirculation areas created by stenoses, aneurysms and bifurcations. In these low shear regions, blood behaves as a non-Newtonian fluid and exhibits shear-thinning, viscoelastic and thixotropic behaviors. Indeed, at low shear rates, molecular mechanisms trigger the aggregation of red blood cells (RBCs) into long column-like structures called “rouleaux”, whereas, at higher shear rates, these structures are deformed, disaggregated and the RBCs re-align in the direction of the flow. This reversible aggregation-disaggregation process is responsible for the shear-thinning behavior of blood. The different timescales of the aggregation and disaggregation processes are at the origin of its thixotropic response. Finally, the viscoelastic properties of blood stem from the elasticity of RBCs and the change of dissipation mechanisms at low and high shear rates [14–18].

Taking into account these complex rheological proprieties in cardiovascular simulations is of critical importance as there exists strong evidence that the non-Newtonian behavior of blood influences the evolution of several cardiovascular pathologies such as atherosclerosis [19]. To that effect, many non-Newtonian constitutive models of blood

* Corresponding author.

E-mail addresses: arthur.ghigo@dalembert.upmc.fr (A.R. Ghigo), pierre-yves.lagree@upmc.fr (P.-Y. Lagrée), fullana@lmm.jussieu.fr, jose.fullana@upmc.fr (J.-M. Fullana).

have been developed and can be roughly categorized as (i) time-independent and (ii) time-dependent models. (i) Time-independent constitutive models describe only the shear-thinning behavior of blood and are particularly relevant in shear-dominated steady flows [20–22]. Due to their simplicity, they are the most commonly used non-Newtonian blood flow models in two-dimensional (2D) and 3D numerical simulations. They have been applied to study blood flow in intracranial aneurysms [23,24], stenoses [25,26], coronary arteries [27], idealized small arterial networks [28–31] and heart valves [32]. (ii) Time-dependent constitutive models account for the viscoelastic and thixotropic properties of blood as well as its shear-thinning behavior in the steady flow limit. Historically, they were developed based on an analogy between blood and a viscoelastic Maxwell material [33]. More recently, a generalized Maxwell model has been derived in [34,35] using polymer network theory, and successive improvements have enabled the description of the Fahraeus and Fahraeus–Lindquist effects, while in [36–39], a generalized Oldroyd-B model has been proposed and improved following a thermodynamics approach. These time-dependent models have been successfully incorporated into 3D simulations [39–43] and good agreement has been found with experimental data in simple steady and pulsatile flows.

However, neither time-independent nor time-depend models have been applied to study 3D blood flow in large vascular networks as the computational and modeling costs of such simulations are prohibitive. Only in [44,45] have the authors considered the non-Newtonian behavior of blood in reduced-order simulations of blood flow in large arterial networks. However, both studies employ time-independent non-Newtonian models which are enabled to describe, in the transient flow conditions often encountered *in vivo*, the viscoelastic and thixotropic properties of blood.

The goal of this work is therefore to couple an accurate time-dependent non-Newtonian model to a 1D blood flow model in order to efficiently describe the hemodynamics in large networks of deformable arteries all the while accounting for the complex rheology of blood. The rheological model we choose is a 1D simplification of an Oldroyd-B model [46] and is consistent with the modeling complexity of the 1D blood flow equations. It involves a viscoelastic Maxwell equation for the wall shear stress, parametrized by wall shear rate and structure-dependent coefficients, and a kinetic equation describing the transport and aggregation-disaggregation of RBCs, which are considered as a homogeneous single phase.

This article is organized as follows. In Section 2, we present the 1D blood flow model, the non-Newtonian shear stress model and its integration into the 1D blood flow model. In Section 3, we describe analytic solutions of the rheological model in different flow conditions, allowing us to exhibit the shear-thinning, thixotropic and viscoelastic behaviors of the model. Then, in Section 4, we compare numerical results of the model to published steady and unsteady experimental rheological data. Finally, in Sections 5 and 6, we investigate the influence of the non-Newtonian model on blood flow in synthetic healthy and pathological arterial networks.

2. One-dimensional time-dependent non-Newtonian blood flow model

In this section, we carefully explicit the constitutive equation describing the behavior of the arterial wall, the 1D equations for blood and the time-dependent non-Newtonian rheological model. We then combine each of these equations to form a closed 1D time-dependent non-Newtonian blood flow model.

2.1. One-dimensional solid model

Following ideas exposed in [47,48], we employ a simplified model to describe the mechanical response of the arterial wall. This model is constructed under the hypotheses that arteries are represented as thin,

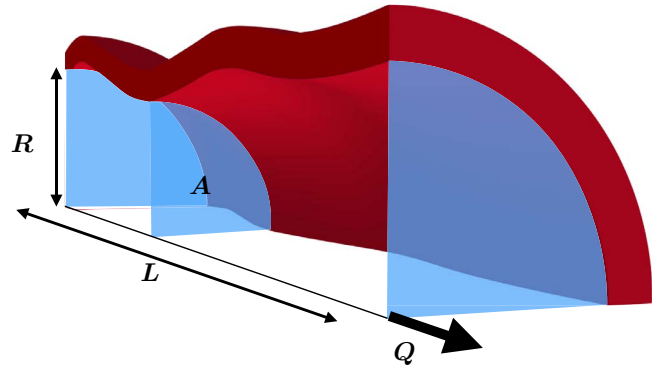


Fig. 1. One-dimensional representation of the fluid domain contained in an axisymmetric cylindrical artery. For clarity, only one-fourth of the artery of length L is represented. The variable Q is the flow rate and $A = \pi R^2$ is the instantaneous cross-sectional area of the artery.

long and straight axisymmetric cylinder (see Fig. 1). Additionally, the arterial wall is described as a homogeneous, isotropic, isothermal and linear elastic material. In this simplified framework, thin-cylinder linear elastic theory provides the following relationship between the transmural pressure variations and the deformation of the arterial wall, describing the spring-like response of the artery [49,50]:

$$p = p_{ext} + K [\sqrt{A} - \sqrt{A_0}]. \quad (1)$$

The variables p and p_{ext} are respectfully the internal and external fluid pressures, A and A_0 are respectfully the instantaneous and the neutral cross-sectional areas and K is the rigidity of the arterial wall.

In the following subsection, we derive 1D equations for the fluid compatible with the constitutive Eq. (1).

2.2. One-dimensional fluid model

Assuming that blood is an incompressible fluid, blood flow in the idealized artery presented in Section 2.1 is described by the 3D incompressible Navier–Stokes equations:

$$\begin{cases} \nabla \cdot \mathbf{u} = 0 & (a) \\ \rho [\partial_t \mathbf{u} + \mathbf{u} \cdot \nabla \mathbf{u}] + \nabla \cdot [p \mathbb{I} - \boldsymbol{\tau}] = 0, & (b) \end{cases} \quad (2)$$

where ρ is the constant fluid density, p is the fluid pressure, $\mathbf{u} = [u_x, u_r, u_\theta]^T$ is the velocity vector written in cylindrical coordinates, \mathbb{I} is the identity tensor and $\boldsymbol{\tau}$ is the stress tensor.

Two physiologically valid hypotheses enable the simplification of the Navier–Stokes Eq. (2). Firstly, in accordance with the geometrical hypotheses made in Section 2.1, the flow is assumed axisymmetric, implying that both the inlet and outlet boundary conditions are also axisymmetric. Secondly, the radius R of the artery is considered small with respect to the wavelength λ_{pulse} of the cardiac pulse wave, which is the characteristic axial length-scale. This assumption is referred to as the long-wave hypothesis and is valid in physiological conditions as $R = 1$ cm and $\lambda_{pulse} = 100$ cm. Combining both hypotheses, the Navier–Stokes Eq. (2) simplify into the reduced Navier–Stokes–Prandtl (RNSP) Eqs. [51], describing the conservation of mass and the balance of axial momentum at time t in the axial and radial positions x and r :

$$\begin{cases} \frac{1}{r} \frac{\partial}{\partial r} [r u_r] + \frac{\partial u_x}{\partial x} = 0 & (a) \\ \frac{\partial u_x}{\partial t} + u_r \frac{\partial u_x}{\partial r} + u_x \frac{\partial u_x}{\partial x} = -\frac{1}{\rho} \frac{\partial p}{\partial x} + \frac{1}{\rho r} \frac{\partial}{\partial r} (r \tau_{rx}) & (b) \\ p(x, r, t) = p(x, t). & (c) \end{cases} \quad (3)$$

As a consequence of the long-wave hypothesis, the pressure p depends only on the axial position x and τ_{rx} is the leading-order shear stress component of $\boldsymbol{\tau}$ in the axial momentum Eq. (3b).

The RNSP Eq. (3) are a rich dynamical system [51,52]. They contain all necessary physical ingredients to describe blood flow in large and small arteries, including the well-known pulsatile Womersley [53] and steady Poiseuille [54,55] flow regimes. However, they remain a complex system of partial differential equations, especially when coupled to equations describing the elastic deformation of the arterial wall [56].

To simplify the coupling between the constitutive Eq. (1) and the fluid equations, we integrate the RNSP Eq. (3) over the cross-sectional area A of the idealized artery described in Section 2.1. Through this exact integration process, we obtain 1D fluid equations describing the conservation of mass and the balance of axial momentum in an axisymmetric artery, expressed at time t in the axial position x :

$$\begin{cases} \frac{\partial A}{\partial t} + \frac{\partial Q}{\partial x} = 0 & (a) \\ \frac{\partial Q}{\partial t} + \frac{\partial}{\partial x} \left[\psi \frac{Q^2}{A} \right] + \frac{A}{\rho} \frac{\partial p}{\partial x} = \frac{2\pi R}{\rho} \tau_{rx} \Big|_{r=R} & (b) \end{cases} \quad (4)$$

The variables A and Q are respectively the instantaneous cross-sectional area and the axial flow rate (see Fig. 1) and are defined as:

$$A = 2\pi \int_{r=0}^R r dr \quad \text{and} \quad Q = 2\pi \int_{r=0}^R u_x r dr, \quad (5)$$

where R is the instantaneous radius of the artery. The nonlinear shape factor ψ is defined as:

$$\psi = 2\pi \frac{A}{Q^2} \int_{r=0}^R r u_x^2 dr, \quad (6)$$

and $\tau_{rx}|_{r=R}$ is the wall shear stress (WSS). The expression for the WSS $\tau_{rx}|_{r=R}$ is provided in the following subsection.

2.3. One-dimensional Newtonian and non-Newtonian rheological models

In this subsection, we propose both a Newtonian and a non-Newtonian interpretation of the relation between the WSS $\tau_{rx}|_{r=R}$ and the wall shear rate (WSR) $\dot{\gamma}|_{r=R}$, tailored to the time-dependent rheological properties of blood flow and compatible with the 1D fluid Eqs. (4).

2.3.1. Wall shear rate

The local WSR $\dot{\gamma}|_{r=R}$ is defined as:

$$\dot{\gamma} \Big|_{r=R} = \left[\frac{\partial u_x}{\partial r} + \frac{\partial u_r}{\partial x} \right]_{r=R}. \quad (7)$$

However, the long-wave approximation, valid in physiological conditions, allows us to simplify expression (7):

$$\dot{\gamma} \Big|_{r=R} \approx \frac{\partial u_x}{\partial r} \Big|_{r=R}. \quad (8)$$

In the following, we drop the subscript $|_{r=R}$ and write the WSS as τ_{rx} and the WSR as $\dot{\gamma}$.

2.3.2. Newtonian wall shear stress model

If blood is described as a Newtonian fluid, the WSS τ_{rx} is simply a linear function of the constant blood viscosity μ_∞ and the WSR $\dot{\gamma}$:

$$\tau_{rx} = \mu_\infty \dot{\gamma}. \quad (9)$$

Eq. (9) is the most commonly used rheological model in 1D blood flow simulations. However, results presented in [3] indicate that non-Newtonian blood properties have a significant impact on the hemodynamics in large arterial networks and must therefore be taken into account.

2.3.3. Non-Newtonian wall shear stress model

Following ideas proposed in [57], we construct a time-dependent non-Newtonian blood rheological model compatible with the 1D framework presented previously and able to describe the viscoelastic,

thixotropic and shear-thinning properties of blood.

As the non-Newtonian properties of blood are intrinsically linked to the presence of RBCs in blood plasma, we first describe the transport of RBCs in the systemic network through a simplified 1D transport equation for the average hematocrit \bar{H} (volume occupied by RBCs in a unit volume of blood) [58,59]:

$$\frac{\partial \bar{H}}{\partial t} + U \frac{\partial \bar{H}}{\partial x} = 0. \quad (10)$$

In Eq. (10), we implicitly assume that RBCs are uniformly distributed in the cross-sectional area of the artery, such that $\partial_r \bar{H} = 0$. More complex transport equations can be considered, taking into account the radial distribution of RBCs, but are out of the scope of the 1D approach described here.

Secondly, we adopt a binary representation of the aggregation state of RBCs, which are either aggregated or disaggregated, and describe the local fraction of aggregated RBCs using a single structure parameter f varying between 0 and 1. Therefore, at any point in the arterial network, the average concentration of aggregated RBCs is $\bar{H}f$ and the average concentration of disaggregated RBCs is $\bar{H}(1-f)$. We represent the time and space evolution of the concentration of aggregated RBCs through a simple phenomenological kinetic equation for $\bar{H}f$, allowing us to account for the thixotropic response of blood [57,60,61]:

$$\frac{\partial}{\partial t} [\bar{H}f] + U \frac{\partial}{\partial x} [\bar{H}f] = \frac{\bar{H}(1-f)}{\lambda_a} - \frac{\bar{H}f}{\lambda_d}. \quad (11)$$

The coefficients λ_a and λ_d are respectfully characteristic aggregation and disaggregation time scales and are defined as:

$$\lambda_a = \text{cst} \quad \text{and} \quad \lambda_d = \frac{1}{\delta |\dot{\gamma}|}, \quad (12)$$

with δ a scaling coefficient. The left-hand side of Eq. (11) describes the transport of aggregated RBCs, whereas the right-hand side of Eq. (11) characterizes the local competition between the natural aggregation of RBCs in the absence of shear and their shear-induced disaggregation. If the hematocrit \bar{H} is constant, Eq. (11) simplifies to:

$$\frac{\partial f}{\partial t} + U \frac{\partial f}{\partial x} = \frac{1-f}{\lambda_a} - \frac{f}{\lambda_d}. \quad (13)$$

Thirdly, using a classic viscoelastic hypothesis [62], we assume that the WSS τ_{rx} is a linear superposition of a structure (or polymeric) shear stress τ_{st} and a Newtonian (or solvent) shear stress:

$$\tau_{rx} = \tau_{st} + \mu_\infty \dot{\gamma}, \quad (14)$$

where μ_∞ is the viscosity of blood in the high WSR asymptotic limit. Following [38,39,57], we then use a viscoelastic Oldroyd-B model [46], involving an upper-convected time derivative, to describe the time and space evolution of τ_{st} . However, in the 1D framework, the advection effects taken into account by the upper-convected time derivative are negligible as the shear stress is maximum at the wall, where the velocity is small. The Oldroyd-B model therefore simplifies into a 1D viscoelastic Maxwell equation, representing the combined contributions of an elastic spring and a viscous dashpot:

$$\lambda_{st} \frac{\partial \tau_{st}}{\partial t} + \tau_{st} = \mu_{st} \dot{\gamma}. \quad (15)$$

The coefficients λ_{st} and μ_{st} are respectfully the characteristic elastic relaxation time and the structure viscosity, simply defined as:

$$\lambda_{st} = \lambda_a f \quad \text{and} \quad \mu_{st} = [\mu_0 - \mu_\infty] f, \quad (16)$$

with μ_0 the viscosity of blood in the low WSR asymptotic limit. Eq. (16) expresses the simplest possible relation between the structure parameter f and blood parameters.

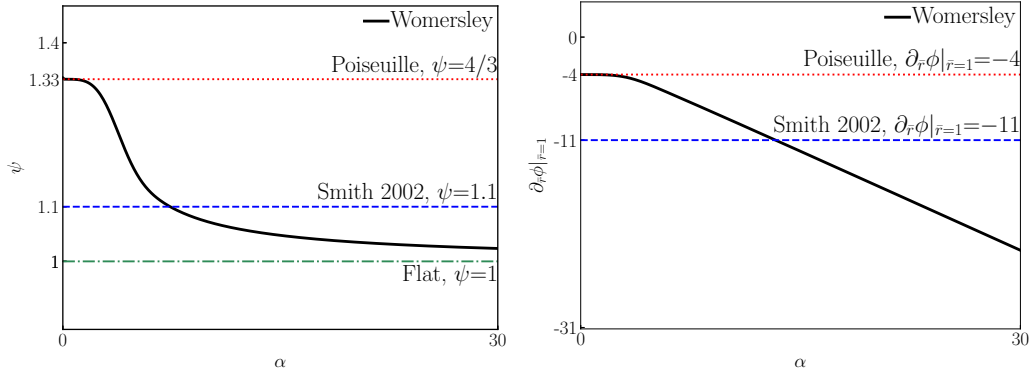


Fig. 2. Evolution of the nonlinear shape factor ψ (left) and the dimensionless WSR $\partial_r\phi|_{r=1}$ (right) computed with the linear Newtonian Womersley velocity profile closure (22) (—). The straight lines correspond to the coefficients obtained by Smith in [68] (—, $\psi = 1.1$, $\partial_r\phi|_{r=1} = -11$), with a Poiseuille profile closure (···, $\psi = 4/3$, $\partial_r\phi|_{r=1} = -4$) and with a flat profile closure (- - -, $\psi = 1$, $\partial_r\phi|_{r=1} = -\infty$).

2.4. Velocity profile closure

In the previous subsections, we have provided equations that describe the 1D time-dependent non-Newtonian blood flow in elastic arteries. However, two unknowns remain, namely the nonlinear advection coefficient ψ and the WSR $\dot{\gamma}$. Both variables dependent on the axial velocity profile u_x , which we have left undefined.

Using classical 1D closure hypotheses [2,63], we express the axial velocity u_x as:

$$u_x(x, r, t) = \phi(\bar{r}, t)U(x, t), \tag{17}$$

where $U = Q/A$ is the average axial velocity, $\bar{r} = r/R(x, t)$ is the dimensionless radial position and ϕ is the dimensionless shape of the velocity profile. Using Eq. (17), we then rewrite the nonlinear shape factor ψ and the WSR $\dot{\gamma}$ as:

$$\psi = 2 \int_0^1 \bar{r}\phi^2 dr \quad \text{and} \quad \dot{\gamma} = \frac{U}{R} \frac{\partial\phi}{\partial\bar{r}} \Big|_{\bar{r}=1}. \tag{18}$$

The average velocity U can be computed using the 1D model (4). However, the shape of the axial velocity profile ϕ is lost in the 1D integration process and remains an unknown of the problem. To compute the variables ψ and $\dot{\gamma}$ and close the 1D blood flow equations, we must therefore assume *a priori* shape of the velocity profile, and this choice significantly affects the computed numerical results [64–66].

To gain insights on the physiological values of ψ and $\dot{\gamma}$, we consider the linear flow of Newtonian blood in a straight elastic artery, for which the shape of the velocity profile is given by the linear Newtonian Womersley solution [53,67]:

$$\phi = \Re\left(\frac{u_x}{U}\right) = \Re\left(\frac{1 - \frac{J_0\left(\frac{3}{i^{\frac{3}{2}}}\alpha\bar{r}\right)}{J_0\left(\frac{3}{i^{\frac{3}{2}}}\alpha\right)}}{1 - F_{10}(\alpha)}\right), \tag{19}$$

where F_{10} is defined as:

$$F_{10}(\alpha) = \frac{2}{i^{\frac{3}{2}}\alpha} \frac{J_1\left(\frac{3}{i^{\frac{3}{2}}}\alpha\right)}{J_0\left(\frac{3}{i^{\frac{3}{2}}}\alpha\right)}, \tag{20}$$

and J_0 and J_1 are the first and second Bessel functions. These expressions are parametrized by the Womersley number α , defined as:

$$\alpha = R_0 \sqrt{\frac{\omega}{\nu}}, \tag{21}$$

where ν is the Newtonian kinematic viscosity of blood and ω is the characteristic frequency of blood flow oscillations. From Eq. (19), we

obtain using the software *Mathematica* the following expressions for ψ and $\partial_r\phi|_{r=1}$:

$$\left\{ \begin{array}{l} \psi = \Re\left(\frac{\left(J_1\left(i^{\frac{3}{2}}\alpha\right)^2 + 2J_0\left(i^{\frac{3}{2}}\alpha\right) \left[J_0\left(i^{\frac{3}{2}}\alpha\right) - \frac{{}_0F_1\left(2, \frac{i\alpha^2}{4}\right)}{\Gamma(2)} \right] \right)}{I_2\left(i^{\frac{1}{2}}\alpha\right)}\right) \tag{a} \\ \frac{\partial\phi}{\partial\bar{r}} \Big|_{\bar{r}=1} = \Re\left(-2 \frac{\Gamma(3) {}_0F_1\left(2, \frac{i\alpha^2}{4}\right)}{\Gamma(2) {}_0F_1\left(3, \frac{i\alpha^2}{4}\right)}\right) \tag{b} \end{array} \right. \tag{22}$$

where ${}_0F_1(a, z)$ is the confluent hypergeometric function, $\Gamma(x)$ is the Gamma function and $I_n(z)$ is the modified Bessel function of the first kind.

In Fig. 2, we plot the variations with the Womersley number α of the coefficients ψ and $\partial_r\phi|_{r=1}$ given by Eq. (22). We notice that the coefficients ψ and $\partial_r\phi|_{r=1}$ vary between the following bounds:

$$\left\{ \begin{array}{l} 1 \leq \psi \leq 4/3 \tag{a} \\ \partial_r\phi|_{r=1} \leq -4 \tag{b} \end{array} \right. \tag{23}$$

We therefore assume that $\psi = 1$, which is a reasonable assumption considering the inequality (23a), especially since nonlinear effects are small in physiological conditions. However, this approximation is valid only in the Newtonian case as we are able to predict the influence of non-Newtonian effects on the shape of the velocity profile. Nevertheless, if we assume that non-Newtonian behavior of blood has a flattening effect on the velocity profile, much like with a Bingham fluid, then the approximation $\psi = 1$ remains valid.

Contrary to the nonlinear advection coefficient ψ , we set the value of $\partial_r\phi|_{r=1}$ on a case-by-case basis, as no clear approximations of $\partial_r\phi|_{r=1}$ can be extracted from Eq. (23b). For example, for a Couette flow $\partial_r\phi|_{r=1} = -1$, for a Poiseuille flow $\partial_r\phi|_{r=1} = -4$ and it is common in large arteries to use $\partial_r\phi|_{r=1} = -11$ [1,65] (see Fig. 2).

2.5. One-dimensional time-dependent non-Newtonian blood flow model

Replacing the pressure p by its expression (1) in the axial momentum Eq. (4b) and setting the nonlinear advection coefficient $\psi = 1$, we obtain the following 1D system of equations describing the conservation of mass and the balance of momentum in an elastic artery:

Table 1
Values of the parameters of the simplified Cross constitutive model taken for [20]

μ_∞ [poise]	μ_0 [poise]	λ_{Cr} [s]
0.05	1.3	8

$$\begin{cases} \frac{\partial A}{\partial t} + \frac{\partial Q}{\partial x} = 0 & (a) \\ \frac{\partial Q}{\partial t} + \frac{\partial}{\partial x} \left[\frac{Q^2}{A} + \frac{K}{3\rho} A^{\frac{3}{2}} \right] = \frac{2\pi R}{\rho} \tau_{rx} & (b) \end{cases} \quad (24)$$

The WSS τ_{rx} is obtained by solving the combination of Eq. (10) and Eq. (11), respectively describing the transport of RBCs and aggregated RBCs, and of the time-dependent non-Newtonian rheological model described by Eqs. (14) and (15). The parameters μ_0 , μ_∞ , λ_a , δ and $\partial_F \phi|_{F=1}$ are constants to be determined using available rheological data.

2.6. Numerical scheme

From a mathematical point of view, system (24) is dominantly hyperbolic. In this hyperbolic framework, the flow is subcritical and shock-like phenomena do not occur as the flow speed is smaller than the wave speed in physiological conditions. To capture the propagation of pulse waves, we solve system (24) using a second-order Adam–Bashforth time-integration scheme coupled to a *finite-volume* kinetic numerical scheme [5,69]. The transport Eqs. (10) and (11) are solved using a classical upwind scheme, where the velocity is provided by the kinetic numerical flux [70]. The rheological system (Eqs. (14) and (15)) is explicitly updated using the same time integration scheme as the hyperbolic system (24). Finally, the treatment of inlet and outlet boundary conditions as well as bifurcations is classical and we refer the readers to [49,69,71] for more details.

3. Analysis of the non-Newtonian stress model

We analyze here the time-dependent behavior of the 1D non-Newtonian stress model (Eqs. (10), (11), (14) and (15)) derived in Section 2.3. To simplify the analysis, we consider idealized flow conditions where we assume that all quantities are independent of the axial position x and that the average hematocrit is constant (typically $\bar{H} = 0.45$), allowing us to decouple the rheological model from the 1D blood flow Eq. (24).

3.1. Steady flow: analogy with the simplified Cross model

We consider a steady flow under a constant WSR $\dot{\gamma}$, for which Eqs. (13) and (15) simplify to:

$$\begin{cases} f_s = \frac{1}{1 + \frac{\lambda_a}{\lambda_d}} & (a) \\ \tau_s = [\mu_0 - \mu_\infty] f_s \dot{\gamma} & (b) \end{cases} \quad (25)$$

where f_s and τ_s are respectively the steady structure parameter and the steady structure shear stress.

This steady state results from the balance between aggregation and disaggregation processes, and the equilibrium value of the structure parameter (25a) explicitly depends on the aggregation time scales λ_a and λ_d :

- if $\lambda_a \gg \lambda_d$ then $f \approx 0$ and shear-induced RBC disaggregation is the dominant mechanism;
- if $\lambda_a \ll \lambda_d$ then $f \approx 1$ and natural RBC aggregation is the dominant mechanism.

Table 2
Parameters of the time-dependent non-Newtonian blood constitutive model, given in cgs units and based on an analogy with the simplified Cross constitutive model [72] and experimental data from [18].

ρ [g·cm ⁻³]	μ_∞ [poise]	μ_0 [poise]	λ_a [s]	δ
1	0.05	1.3	5	1.5

Additionally, we can explicitly define the apparent viscosity $\mu = \frac{\tau_{rx}}{\dot{\gamma}}$ using Eqs. (14), (25a) and (25b):

$$\mu = \mu_\infty + \frac{\mu_0 - \mu_\infty}{1 + \frac{\lambda_a}{\lambda_d}} \quad (26)$$

The apparent viscosity (26) exhibits the expected shear-thinning behavior and is formally identical to the simplified Cross constitutive model [72]:

$$\mu = \mu_\infty + \frac{\mu_0 - \mu_\infty}{1 + \lambda_{Cr} \dot{\gamma}} \quad (27)$$

In Table 1, we summarize the values of the parameters of the simplified Cross constitutive model taken from [20]. Thanks to the analogy between the apparent viscosity (26) and the Cross viscosity (27), we use the values of μ_0 and μ_∞ presented in Table 1 and determine the remaining unknown parameters λ_a and δ using the value of the constant λ_{Cr} and experimental data presented in [18]. The complete set of parameters of the rheological model is presented in Table 2.

3.2. Constant wall shear rate

We now study the disaggregation under a constant WSR $\dot{\gamma}$ of blood initially at rest. At $t = 0$, we assume that $f = 1$ and $\tau_{st} = 0$. The kinetic equation for the structure parameter is:

$$\frac{df}{dt} = \frac{1-f}{\lambda_a} - \frac{f}{\lambda_d}, \quad (28)$$

and its solution is:

$$f = f_s + [1 - f_s] e^{-\frac{t}{\lambda_c}}, \quad (29)$$

where $1/\lambda_c = 1/\lambda_a + 1/\lambda_d$. Injecting expression (29) in Eq. (15), we obtain the following expression for the structure shear stress τ_{st} :

$$\tau_{st} = \tau_s \frac{[1 - f_s] \frac{t}{\lambda_a} + f_s^2 \left[e^{\frac{t}{\lambda_c}} - 1 \right]}{f_s + f_s^2 \left[e^{\frac{t}{\lambda_c}} - 1 \right]} \quad (30)$$

The analysis of Eqs. (29) and (30) allows us to highlight two different temporal dynamics described by the rheological model:

- an asymptotic viscoelastic dynamic when $t \rightarrow \infty$. Indeed, at very long times, the structure parameter f and the structure shear stress τ_{st} converge towards the steady values presented in Section 3.1:

$$\begin{cases} f_{t \rightarrow \infty} = f_s & (a) \\ \tau_{st, t \rightarrow \infty} = \tau_s & (b) \end{cases} \quad (31)$$

This asymptotic behavior highlights the viscoelastic transition from an initially aggregated state ($f = 1$, $\tau_{st} = 0$) towards a steady equilibrium state (system (31)) where aggregation and disaggregation are perfectly balanced.

- a thixotropic temporal dynamic at intermediate times $0 < t < \infty$. Indeed, for given values of λ_a and λ_d , it is possible to find the analytic expression for the time $t_{\tau_{st}, \max}$ at which the maximum value of τ_{st} (30) is reached:

$$t_{st,max} = \lambda_c \left[1 + \frac{1}{1 - \frac{\lambda_c}{\lambda_a}} + W \left(\left[\frac{\lambda_a}{\lambda_c} - 1 \right] e^{-\left[1 + \frac{1}{1 - \frac{\lambda_c}{\lambda_a}} \right]} \right) \right] \quad (32)$$

with:

$$\tau_{st,max} = \tau_s \left[1 + W \left(\left[\frac{\lambda_a}{\lambda_c} - 1 \right] e^{-\left[1 + \frac{1}{1 - \frac{\lambda_c}{\lambda_a}} \right]} \right) \right] \quad (33)$$

The function W is the *Lambert-W* function, which is the inverse function of $f(w) = we^w$. Using expressions (32) and (33), simple calculations allow us to show that $0 < t_{st,max} < \infty$ and that $\tau_{st,max} \geq \tau_s$. We can therefore conclude that in this configuration, the structure shear stress τ_{st} exhibits a thixotropic behavior at finite times, represented by an overshoot with respect to the asymptotic steady value τ_s . The magnitude of the overshoot depends on the value of the characteristic aggregation timescales λ_a and λ_d :

★ if $\lambda_a \gg \lambda_d$ (equivalently $\dot{\gamma} \gg 1 \text{ s}^{-1}$), then $\lambda_c \approx \lambda_d$ and we have:

$$\tau_{st,max} \gg \tau_s \quad (34)$$

In this case, disaggregation occurs at a much smaller timescale than aggregation due to the high WSR value. This results in large variations of the structure of blood at small times ($t \leq \lambda_c$) and therefore a large thixotropic overshoot of the structure shear stress τ_{st} before the system relaxes towards the steady structure shear stress τ_s .

★ if $\lambda_a \ll \lambda_d$ (equivalently $\dot{\gamma} \ll 1 \text{ s}^{-1}$), then $\lambda_c \approx \lambda_a$ and we have:

$$\tau_{st,max} \approx \tau_s \quad (35)$$

In this case, aggregation occurs at a much smaller timescale than disaggregation due to the low WSR value. This results in almost no variation of the structure of blood and therefore no thixotropic overshoot of the structure shear stress τ_{st} .

3.3. Zero wall shear rate

We study here the reaggregation of initially disaggregated blood in the absence of shear ($\dot{\gamma} = 0$). At $t = 0$, we assume that $f = f_0$ and $\tau_{st} = \tau_{st,0}$. The kinetic equation for the structure parameter is:

$$\frac{df}{dt} = -\frac{1+f}{\lambda_a} \quad (36)$$

and its solution is straightforward:

$$f = 1 + [f_0 - 1]e^{-\frac{t}{\lambda_a}} \quad (37)$$

Injecting expression (37) in Eq. (15), we obtain the following expression for the structure shear stress τ_{st} :

$$\tau_{st} = \tau_{st,0} \frac{f_0}{f_0 - 1 + e^{\frac{t}{\lambda_a}}} \quad (38)$$

Eqs. (37) and (38) enable us to highlight another asymptotic viscoelastic temporal dynamic when $t \rightarrow \infty$. Indeed, at very long times, the structure parameter f and the structure shear stress τ_{st} relax towards the steady values presented in Section 3.1, computed here for $\dot{\gamma} = 0$:

$$\begin{cases} f_{t \rightarrow \infty} = 1 & (a) \\ \tau_{st,t \rightarrow \infty} = 0 & (b) \end{cases} \quad (39)$$

This asymptotic behavior highlights the viscoelastic relaxation of initially disaggregated RBCs towards a fully aggregated state. The phenomenon is driven only by the characteristic aggregation timescale λ_a as in the absence of shear $\lambda_d \rightarrow \infty$.

The asymptotic analysis conducted in this section highlights the

shear-thinning, viscoelastic and thixotropic behaviors of the proposed rheological model (Eqs. (10), (11), (14) and (15)). In the following sections, we compare numerical results, where spatial and hematocrit variations taken into account, to the analytic results previously obtained and to experimental results in order to assess if the model is able to quantitatively describe time-dependent non-Newtonian behaviors of blood.

4. Comparison with experimental data

We propose to compare here the numerical results of the 1D non-Newtonian blood flow model to experimental data available in the literature. We use published results of Barbee [73], Bureau et al. [17] and McMillan et al. [74], where the authors systematically studied the steady behavior of blood in a capillary viscometer and its unsteady response to step and triangular shear solicitations using a coaxial cylinder microviscosimeter.

In each example, we reproduce the viscometric conditions of the experiment by imposing similar shear rate conditions in a straight artery of length L , neutral radius R_0 and rigidity K . To do so, we impose the flow rate Q_{in} at the inlet of the artery and a homogeneous Neumann boundary condition for the flow rate at the outlet of the artery. We also impose a constant average hematocrit $\bar{H} = 0.45$ and homogeneous Neumann boundary conditions for the structure parameter f at the inlet and outlet of the artery. The time-evolution of the inlet flow rate Q_{in} depends on the considered experimental test case and is designed to impose a chosen WSR $\dot{\gamma}_{in}$:

$$Q_{in}(\dot{\gamma}_{in}) = \dot{\gamma}_{in} \left[\frac{\partial \phi}{\partial r} \Big|_{r=1} \right]^{-1} A_0 R_0, \quad (40)$$

where A_0 is the neutral cross-sectional area of the artery. Finally, each simulation is initialized by the following initial conditions:

$$\begin{cases} Q = 0 & \text{and} & A = A_0 & (a) \\ \bar{H} = 0.45 & \text{and} & f = 1 & \text{and} & \tau_{st} = 0 & (b) \end{cases} \quad (41)$$

The parameters of the time-dependent non-Newtonian blood constitutive model are summarized in Table 2, the geometrical and mechanical parameters describing the artery in Table 3 and the time- and space-discretization parameters in Table 4.

4.1. Steady state

In [73], Barbee obtained, using a capillary viscometer, the evolution of the steady shear rate as a function of the pseudo shear rate $\bar{U} = U/[2R]$ for 9 different blood samples with different hematocrit values.

In Fig. 3, we compare these experimental results to steady numerical results computed with the 1D non-Newtonian blood flow model and to the steady analytic solution obtained in Section 3.1 (Eq. (25)). We notice that, as expected, the analytic and 1D numerical results are perfectly matched. Moreover, we observe that the results predicted by the 1D non-Newtonian blood flow model are well within the experimental data range and describe blood with an average hematocrit $0.345 \leq \bar{H} \leq 0.500$.

To better fit the experimental data of Barbee [73], we could have taken into account the dependence of the viscosities μ_0 and μ_∞ with the average hematocrit \bar{H} and the blood temperature, following approaches proposed in [22,59]. Similarly, we could also have accounted

Table 3
Geometrical and mechanical parameters describing the artery, given in cgs units.

L [cm]	A [cm ²]	K [dyne·cm ⁻³]	$\partial_r \phi _{r=1}$
10	1	10 ⁴	-4

Table 4
Numerical parameters describing the time discretization and the mesh.

Δt [s]	Δx [cm]	Order
10^{-4}	5×10^{-2}	2

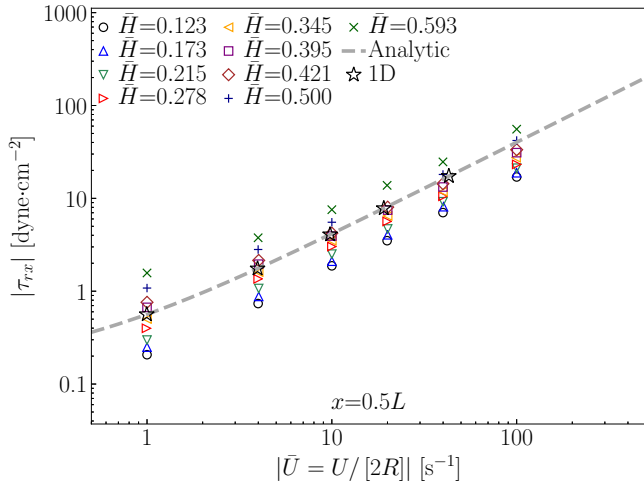


Fig. 3. Evolution of the WSS τ_{rx} with the pseudo shear rate $\bar{U} = U/[2R]$: comparison between experimental data from Barbee [75] for different hematocrit values (marks), steady results of the 1D non-Newtonian blood flow model (*) and the steady analytic solution (25) (—). The analytic and 1D numerical results are perfectly matched and are well within the experimental data range, describing blood with an average hematocrit $0.345 \leq \bar{H} \leq 0.500$.

for the dependence of blood parameters with the average fibrinogen concentration \bar{c}_f [22,76]. However, taking into account such detailed parametric dependence would have been inconsistent with the level of approximation of the 1D blood flow equations and is therefore out of the scope of the 1D approach described here.

This comparison with steady experimental data highlights the shear-thinning behavior of the 1D non-Newtonian blood flow model in the steady flow limit. Moreover, these results show that with a minimal number of parameters, the 1D non-Newtonian blood flow model is able to reproduce average steady rheological data.

4.2. Single shear-step

In a series of experiments, Bureau et al. [77] obtained experimental

data on the behavior of a blood sample subjected to the following step-change in shear rate:

$$\dot{\gamma}(t) = \begin{cases} \dot{\gamma}_{1,2} & \text{for } 0 \leq t < \Delta t_{1,2} \\ 0 & \text{for } \Delta t_{1,2} \leq t. \end{cases} \quad (42)$$

To highlight separately the viscoelastic and thixotropic behaviors of blood, Bureau et al. considered a low shear rate regime for which ($\dot{\gamma}_1 = 0.05 \text{ s}^{-1}$ and $\Delta t_1 = 30 \text{ s}$) and a high shear rate regime ($\dot{\gamma}_2 = 1 \text{ s}^{-1}$ and $\Delta t_2 = 8.5 \text{ s}$).

In Fig. 4, we compare the time evolution of the measured experimental shear stress to the computed 1D numerical WSS and to the analytic solutions presented in Sections 3.2 and 3.3 (Eqs. (30) and (38)). We observe that for both flow conditions $\dot{\gamma}_1$ and $\dot{\gamma}_2$, the experimental data from Bureau et al. [77] agree qualitatively and semi-quantitatively with the 1D numerical results. Moreover, the analytic and 1D numerical results are perfectly matched. The data presented in Fig. 4 Left are characteristic of a viscoelastic material: the shear stress rises monotonously towards an equilibrium steady value and then relaxes in the absence of shear towards a fully aggregated state. On the contrary, the data plotted in Fig. 4 Right present the characteristic overshoot of a thixotropic material. Both rheological behaviors are described in Section 3.2 and can be explained focusing on the evolution of the structure parameter f , presented in Fig. 5. Indeed, in the low shear rate regime ($\dot{\gamma}_1$), the structure of blood is not significantly altered. Whereas in the high shear rate regime ($\dot{\gamma}_2$), large variations of the structure of blood occur on a short timescale, leading to memory effects and a thixotropic overshoot of the shear stress.

The agreement with experimental data from Bureau et al. [77] observed here indicates that the 1D non-Newtonian blood flow model enables, with a minimal number of parameters, a satisfactory description of the viscoelastic and thixotropic time-dependent behaviors of blood.

4.3. Multiple shear-steps

Experimental data from McMillan et al. [74] describe the time-dependent shear stress response of blood to two successive shear-steps of amplitude $\dot{\gamma} = 8 \text{ s}^{-1}$ and of length $\Delta t = 2.5 \text{ s}$. The experiment was repeated three times, each time decreasing the time delay Δt_d between the consecutive shear-steps, during which no shear was applied.

In Fig. 6 Left, we compare the time evolution of the experimental and 1D numerical shear stresses for different time delays $\Delta t_d \in \{1.5, 1, 0.5\}$. Both solutions are qualitatively and quantitatively comparable and we observe the expected viscoelastic relaxation and thixotropic transient overshoot. Results in Fig. 6 Right correlate the

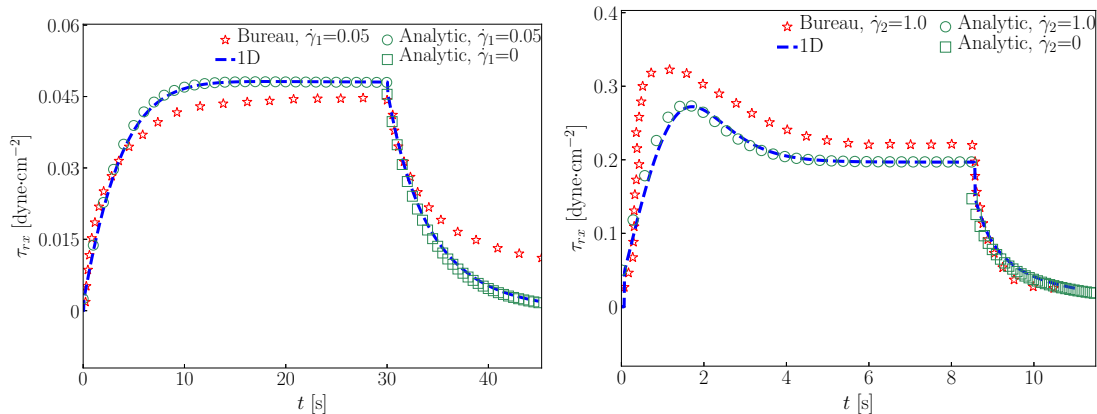


Fig. 4. Time evolution of the shear stress τ_{rx} with a step-change in shear rate: comparison between experimental data from Bureau [77] et al. (☆), results of the 1D non-Newtonian blood flow model (—) and analytic solutions (30) (○) and (38) (□). **Left:** Low shear rate viscoelastic regime with $\dot{\gamma}_1 = 0.05 \text{ s}^{-1}$ for $\Delta t_1 = 30 \text{ s}$ and then $\dot{\gamma}_1 = 0 \text{ s}^{-1}$. **Right:** High shear rate thixotropic regime (overshoot) with $\dot{\gamma}_2 = 1 \text{ s}^{-1}$ for $\Delta t_2 = 8.5 \text{ s}$ and then $\dot{\gamma}_2 = 0 \text{ s}^{-1}$. There is a qualitative and quantitative match between experimental data and numerical results, and a perfect match between analytic and numerical results.

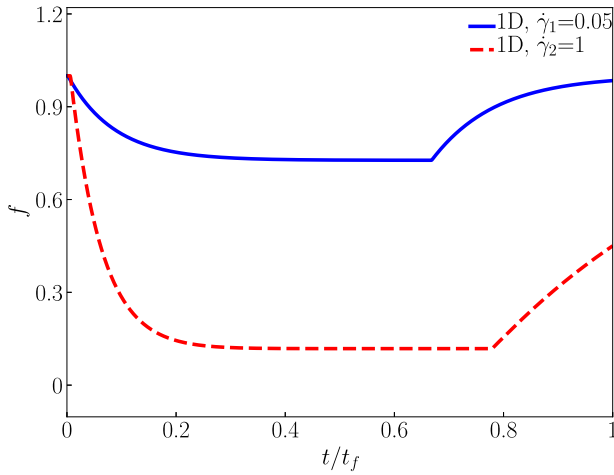


Fig. 5. Time evolution of the structure parameter f with a step-change in shear rate, computed using the 1D non-Newtonian blood flow model: (—) low shear rate viscoelastic regime with $\dot{\gamma}_1 = 0.05 \text{ s}^{-1}$ for $\Delta t_1 = 30 \text{ s}$; (---) high shear rate thixotropic regime with $\dot{\gamma}_2 = 1 \text{ s}^{-1}$ for $\Delta t_2 = 8.5 \text{ s}$. In the high shear regime, there is a large decrease of the structure parameter f on a short timescale, leading to the thixotropic behavior observed in Fig. 4 Right.

increase of the overshoot amplitude with larger variations of the structure parameter f , as blood has more time to reaggregate when Δt_d increases.

4.4. Triangle shear solicitation

Bureau *et al.* [17] also obtained experimental hysteresis curves by imposing the following triangular shear rate solicitation on the blood sample:

$$\dot{\gamma}(t) = \begin{cases} \dot{\gamma}_{1,2} \frac{t}{t_{1,2}} & \text{for } 0 \leq t < t_{1,2} \\ \dot{\gamma}_{1,2} \left[2 - \frac{t}{t_{1,2}} \right] & \text{for } t_{1,2} \leq t \leq 2t_{1,2}. \end{cases} \quad (43)$$

To highlight the viscoelastic and thixotropic behaviors of blood, the authors considered a low shear rate regime ($\dot{\gamma}_1 = 0.12 \text{ s}^{-1}$ and $t_1 = 13 \text{ s}$) and a high shear rate regime ($\dot{\gamma}_2 = 1.03 \text{ s}^{-1}$ and $t_2 = 47.6 \text{ s}$).

In Fig. 7, we plot the experimental and numerical variations of the shear stress τ_{rx} with respect to the shear rate $\dot{\gamma}$. In the low shear rate regime $\dot{\gamma}_1$ plotted in Fig. 7 Left, the viscoelastic behavior of blood is highlighted and the experimental and numerical results match very well. In the high shear rate regime displayed on Fig. 7 Right, the

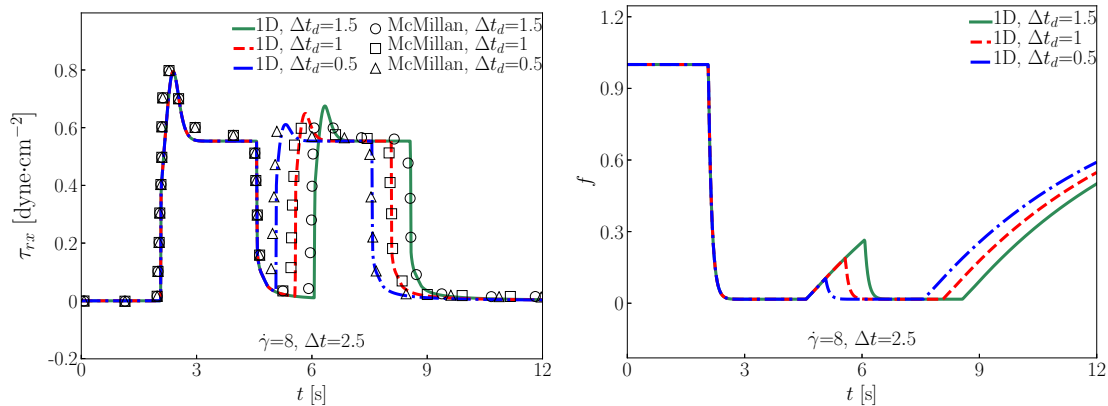


Fig. 6. Time evolution of the shear stress τ_{rx} (left) and the structure parameter f (right) with two successive step-changes in shear rate of amplitude $\dot{\gamma} = 8 \text{ s}^{-1}$ and of length $\Delta t = 2.5 \text{ s}$: comparison between experimental data from McMillan *et al.* [74] and numerical results of the 1D non-Newtonian blood flow model for a time delay $\Delta t_d \in \{1.5 \text{ (exp. 0, 1D —)}, 1 \text{ (exp. □, 1D ---)}, 0.5 \text{ (exp. △, 1D - - -)}\} \text{ s}$. There is a qualitative and quantitative agreement between experimental and numerical data. The thixotropic overshoot increases with Δt_d as structure variations are more important.

thixotropic effect is dominant. For the increasing shear region of the curve, the experimental and numerical results are well matched. However, for the decreasing shear part, the experimental results are not well reproduced, even though shear stress amplitudes are similar.

The results presented in Sections 4.1–4.4 indicate that the 1D non-Newtonian blood flow model allows us to compute numerical results similar to well-known experimental data form [73,74,77,77]. We can now move towards more complex simulations in large networks of elastic arteries.

5. Elementary bifurcation

Bifurcations are elementary parts of an arterial network and connect a parent artery p to two daughter arteries d_1 and d_2 . Bifurcations are responsible for the reflection of the incoming pulse wave as they represent impedance discontinuities in the network. Moreover, due to the complex flow patterns they generate, the non-Newtonian behavior of blood can be particularly important in these configurations.

In a symmetric bifurcation, we compare the results of the 1D non-Newtonian blood flow model to those of its Newtonian counterpart. The geometrical and mechanical properties of the bifurcation are presented in Table 5 and correspond to the average properties of large arteries. At the inlet of the parent artery p , we impose the flow rate Q_{in} to mimic the behavior of the heart:

$$Q_{in}(t) = Q_h \max\left(0, \sin\left(2\pi \frac{t}{T_h}\right)\right), \quad 0 \leq t \leq 5T_h, \quad (44)$$

with $T_h = 1 \text{ s}$. We choose the maximum flow rate $Q_h \in \{1, 10, 100\} \text{ cm}^3 \text{ s}^{-1}$ to describe the flow in different regions of the systemic network. We also impose a constant average hematocrit $\bar{H} = 0.45$ and homogeneous Neumann boundary conditions for the structure parameter f at the inlet and outlet of each artery. At the outlet of the daughter arteries d_1 and d_2 , we set non-reflecting boundary conditions. Finally, the initial conditions are (41) and the time- and space-discretization parameters of the network are described in Table 4. We present data obtained after 4 periods to ensure that the system has reached a periodic state.

In Fig. 8, we compare the waveforms for the structure parameter f (left), shear stress τ_{rx} (middle) and pressure p (right), computed with the Newtonian and non-Newtonian 1D blood flow models. Numerical data are taken in the middle of the parent artery p and the daughter artery d_1 , and we do not present results for the artery d_2 as they are identical to those of artery d_1 . As we decrease the flow rate ($Q_h = 100 \text{ cm}^3 \text{ s}^{-1}$ to $Q_h = 1 \text{ cm}^3 \text{ s}^{-1}$ from top to bottom in Fig. 8), the shear rate decreases, allowing the RBCs to aggregate. Consequently, in both parent and daughter arteries, the structure parameter f and the shear stress $|\tau_{rx}|$ are larger in the non-Newtonian than in the Newtonian case,

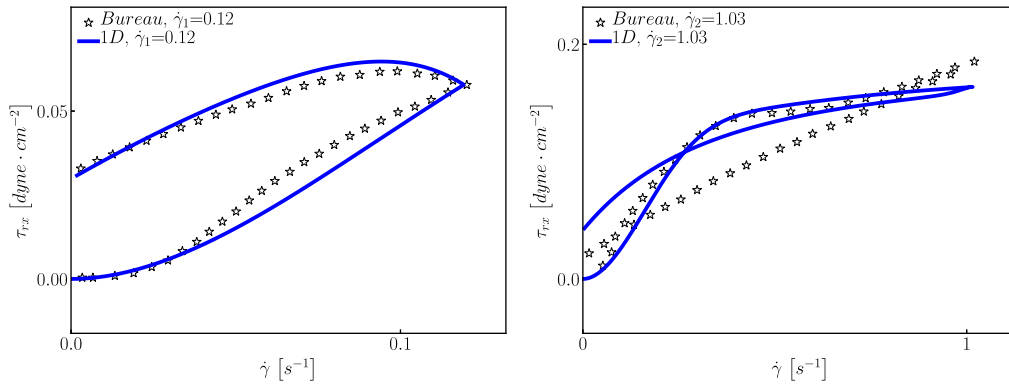


Fig. 7. Hysteresis curves of the evolution of the shear stress τ_{rx} as a function of the shear rate $\dot{\gamma}$ under a triangular shear solitation: comparison between experimental data from Bureau [17] (\star) and 1D numerical results (—). **Left:** Low shear viscoelastic regime with $\dot{\gamma}_1 = 0.12 \text{ s}^{-1}$ and $t_1 = 13 \text{ s}$. **Right:** High shear thixotropic regime with $\dot{\gamma}_2 = 1.03 \text{ s}^{-1}$ and $t_2 = 47.6 \text{ s}$. There is a qualitative and quantitative match between experimental data and numerical results.

with up to 100% differences for $Q_h = 1 \text{ cm}^3 \text{ s}^{-1}$. The pressure then rises to compensate the increased viscous stresses and maintain the normal flow. Note that the value of f is higher and the value of $|\tau_{rx}|$ is lower in artery d_1 than in artery p as the flow coming from artery p splits in two to vascularize both daughter arteries.

These results indicate that in the elementary network considered here, non-Newtonian effects can lead to modifications of the WSS stress patterns and an increase of pressure. These results are corroborated by similar data obtained in different 3D studies [27,30] of bifurcations. In the following, we extend this analysis to non-Newtonian effects in large networks of arteries.

These results indicate that in the elementary network considered

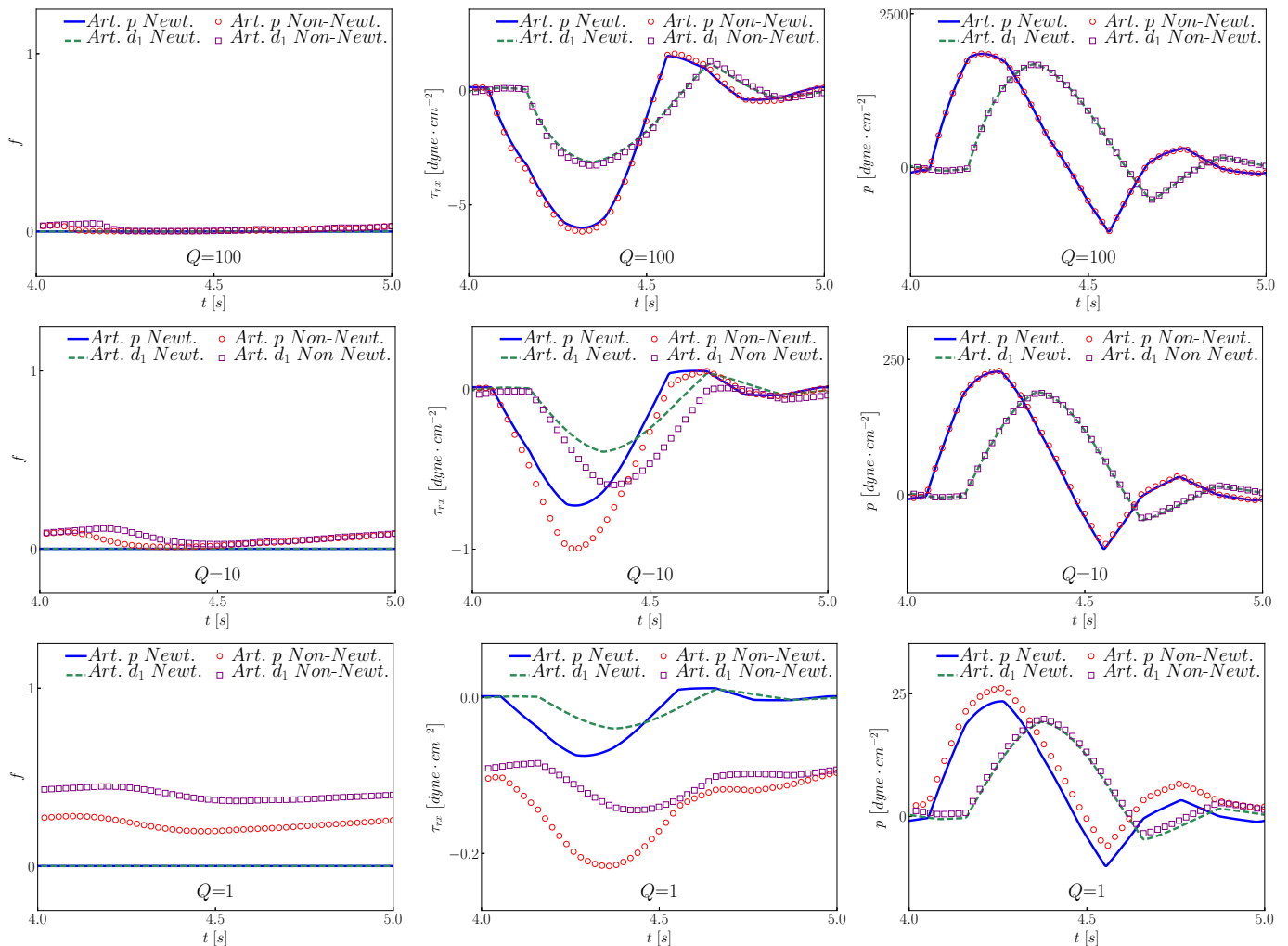


Fig. 8. Temporal evolution of the structure parameter f (left), the shear stress τ_{rx} (middle) and the pressure p (right) taken in the middle of the parent artery p and the daughter artery d_1 . **Top:** $Q_h = 100 \text{ cm}^3 \text{ s}^{-1}$. **Center:** $Q_h = 10 \text{ cm}^3 \text{ s}^{-1}$. **Bottom:** $Q_h = 1 \text{ cm}^3 \text{ s}^{-1}$. We compare the results of the Newtonian (artery p —, artery d_1 —) and the non-Newtonian (artery p \circ , artery d_1 \square) 1D blood flow models. As the flow rate decreases, the aggregation increases, leading to a higher shear stress $|\tau_{rx}|$ and an increase of the pressure p .

6. Idealized asymmetric network

Reduced-order 1D blood flow models have been designed to capture the wave propagation dynamics in large networks. We therefore analyze here how non-Newtonian effects affect the network hemodynamics using the 1D time-dependent non-Newtonian model presented and validated previously.

We consider an idealized asymmetric arterial tree made only of elementary bifurcations linked together to form a network. In each elementary bifurcation a parent artery p connects to two daughter arteries d_α and d_β . Given the mechanical and geometrical properties of the parent artery p , we construct the daughter arteries using the relationships presented in [78,79] and used more recently in [44,80], which describe the physiological evolution the arteries' geometrical and mechanical properties along the network:

$$\begin{cases} R_\alpha = \alpha R_p & (a) \\ R_\beta = \beta R_p & (b) \\ L = 50R & (c) \\ K = \frac{4}{3} \frac{R}{\sqrt{\rho i}} [k_1 e^{k_2 R} + k_3] & (d) \\ \dot{\gamma} = -4 \frac{U}{R}, & (e) \end{cases} \quad (45)$$

where $\alpha = 0.9$ and $\beta = 0.6$ are asymmetry coefficients and $k_1 = 2 \times 10^7$ dyne cm^{-4} , $k_2 = -22.53 \text{ cm}^{-1}$ and $k_3 = 8.65 \times 10^5$ dyne cm^{-4} . The aim of this study is to understand how the size of the network, dependent on the level n_l of vessel ramifications, influences the aggregation process.

For a given value of n_l , we construct the network by adding the corresponding number n_b of bifurcations and the number n_a of arteries. Table 6 presents the values of n_a and n_b for different values of n_l . At the root of the network, the radius of the artery is $R_0 = 1 \text{ cm}$ and we impose the same pulsatile flow rate (44) as in the previous Section 5, with $Q_h = 100 \text{ cm}^3 \text{ s}^{-1}$ and $T_h = 1 \text{ s}$. We also impose a constant average hematocrit $\bar{H} = 0.45$ and homogeneous Neumann boundary conditions for the structure parameter f at the inlet and outlet of each artery. At the end of each terminal vessel, we set as in the previous section a non-reflecting boundary conditions. We detach ourselves from classical resistive boundary conditions and construct the network dynamics by adding successive levels of vessel ramifications. These boundary conditions are invariant with n_l and provide the adequate framework to study network-size effects. Finally, the initial conditions are (41) and the time- and space-discretization parameters of the network are described in Table 7. We present data obtained after 9 periods to ensure that the system has reached a periodic state.

6.1. Healthy network

We construct three healthy networks with $n_l \in \{2, 4, 6\}$. In Fig. 9, we plot the distribution of the structure parameter f in the three networks at 4 characteristic times of the last cardiac cycle: the beginning $t_1 = 9T_h$, the systolic peak $t_2 = 9.25T_h$, the middle $t_3 = 9.5T_h$ and the diastolic peak $t_4 = 9.75T_h$.

We observe clear effects of network size and asymmetry on the aggregation of RBCs. At $t = 9T_h$, the aggregation is high for $n_l = 2$, as the reflective behavior of the network is smaller due to the smaller number of bifurcations. At $t = 9.25T_h$, the inlet flow rate reaches its maximum value and blood is globally disaggregated for $n_l = \{2, 4, 6\}$.

Table 5

Geometrical and mechanical parameters describing the properties of the parent artery p and the daughter arteries d_1 and d_2 , given in cgs units.

L_{p,d_1,d_2} [cm]	R_{p,d_1,d_2} [cm]	K_{p,d_1,d_2} [dyne cm^{-3}]
10	1	10^4

Table 6

Number n_l of level of vessel ramifications, number n_b of bifurcations and number n_a of arteries of an idealized asymmetric network.

n_l	n_b	n_a
2	3	7
4	15	31
6	63	127
n	$2^n - 1$	$2^{n+1} - 1$

Table 7

Numerical parameters describing the time discretization and the mesh.

Δt [s]	Δx [cm]	Order
10^{-5}	10^{-2}	2

Nevertheless, for $n_l = 4$ and $n_l = 6$, aggregated regions remain in the left hand side (l.h.s.) large extremity arteries. These regions belong to high ramification levels and have not yet been reached by the incoming pulse wave. At $t = 9.5$, all RBCs have been disaggregated by the incoming pulse. Finally at $t = 9.75$, RBCs reaggregate in the l.h.s. large arteries since there is no flow coming from the heart and the reflected waves have been damped by viscous effects. Furthermore, the shear rate $\dot{\gamma}$ is lower in these larger arteries. Overall, aggregation dynamics depend on the size and asymmetry of the network and aggregation occurs principally in the large arteries of the l.h.s. and their immediate daughter arteries. In these arteries, the structure parameter reaches the critical value of $f \approx 0.1$, at which blood displays viscoelastic and thixotropic effects (see Section 4.3).

These results indicate that we must take into account non-Newtonian effects in networks presenting large arteries or a high level of vessel ramifications. Furthermore, these results highlight the importance of the network topology as the asymmetry here influences the aggregation dynamics.

6.2. Pathological network

In the literature, non-Newtonian blood effects have been particularly studied in elementary pathological networks such as bifurcations [27,30,81]. However, as observed before, the size and asymmetry of the network appear to play an important role in the aggregation dynamics. To characterize how pathologies can modify blood flow and aggregation processes in a large network, we introduce two severe stenoses of 90% of obstruction in the 3 networks previously described. One stenosis is located on the l.h.s., in the large radius branch of the network and the other is on the r.h.s, in the small radius branch. The exact position of both stenoses is represented in Fig. 10 by circles (O).

As previously, we plot in Fig. 10 the distribution of the structure parameter f in the three networks ($n_l \in \{2, 4, 6\}$) for the last cardiac cycle: $t_1 = 9T_h$, $t_2 = 9.25T_h$, $t_3 = 9.5T_h$ and $t_4 = 9.75T_h$. For $n_l \in \{4, 6\}$, the presence of the stenoses results in a higher blood aggregation in the arteries downstream of the stenoses compared to Fig. 9. On the contrary for $n_l = 2$, the value of the structure f is lower than in Fig. 9 as the stenoses create reflections that contribute to the disaggregation process. The results show that aggregation effects are amplified in pathological networks as the flow is reduced downstream of the stenoses. Upstream of the stenoses, aggregation is reduced due to additional reflected waves produced by the stenoses.

The numerical results presented in this section demonstrate that non-Newtonian behaviors exist in healthy and pathological networks. Even if these non-Newtonian behaviors are small, they are non-negligible. They affect in particular the WSS distribution in the networks, which plays an important role in cardiovascular pathogenesis. The non-Newtonian aspect of blood must therefore be taken into account to

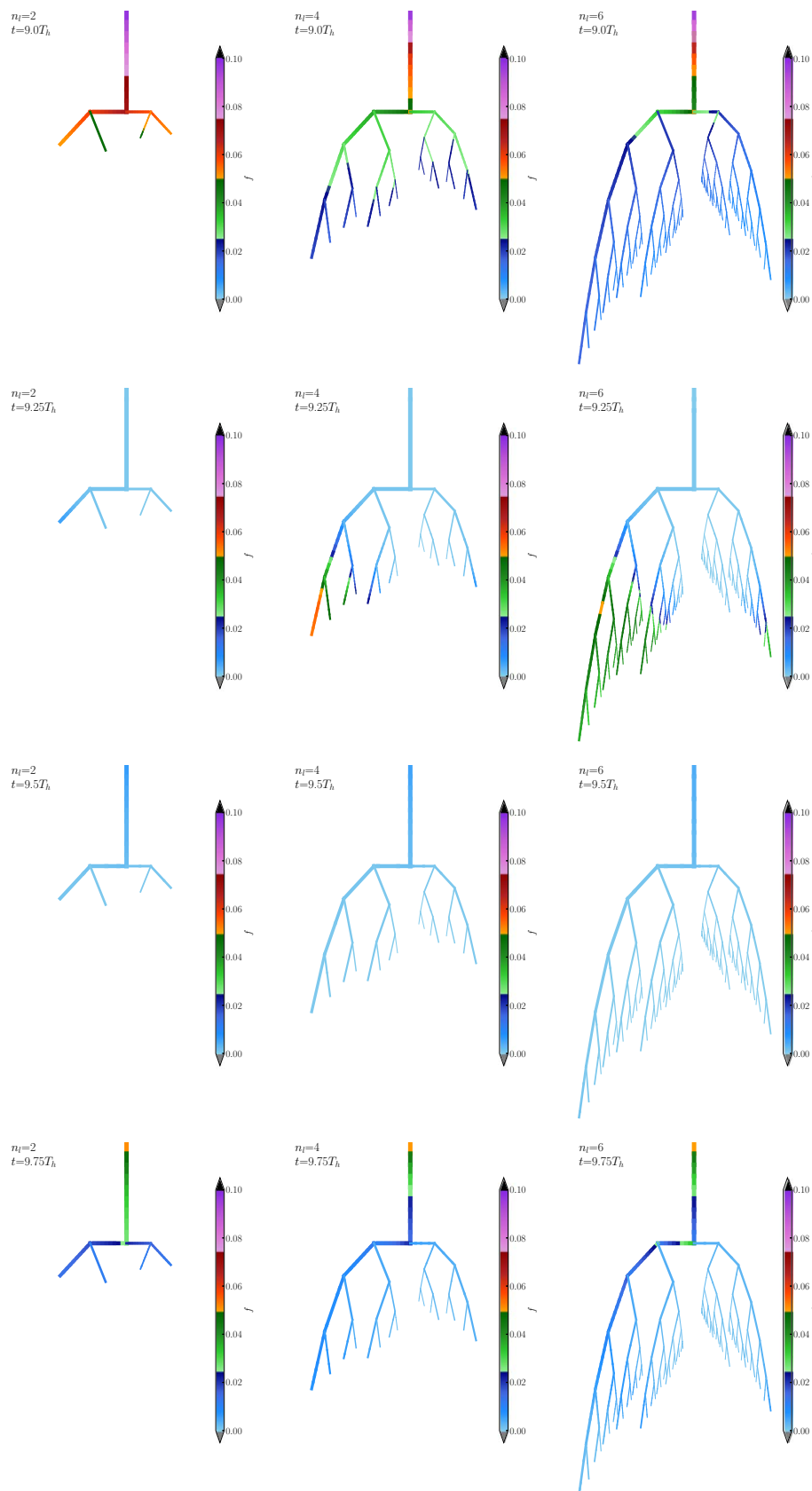


Fig. 9. Snapshots at $t_1 = 9T_h$, $t_2 = 9.25T_h$, $t_3 = 9.5T_h$ and $t_4 = 9.75T_h$ of the distribution of the structure parameter f in three networks with increasing levels of ramification $n_i \in \{2$ (left), 4 (middle), 6 (right) $\}$. Aggregation occurs mainly in the large arteries on the l.h.s of the network and in their immediate daughter arteries. Aggregation depends on the pulsatility of the flow, the size and the asymmetry of the network.

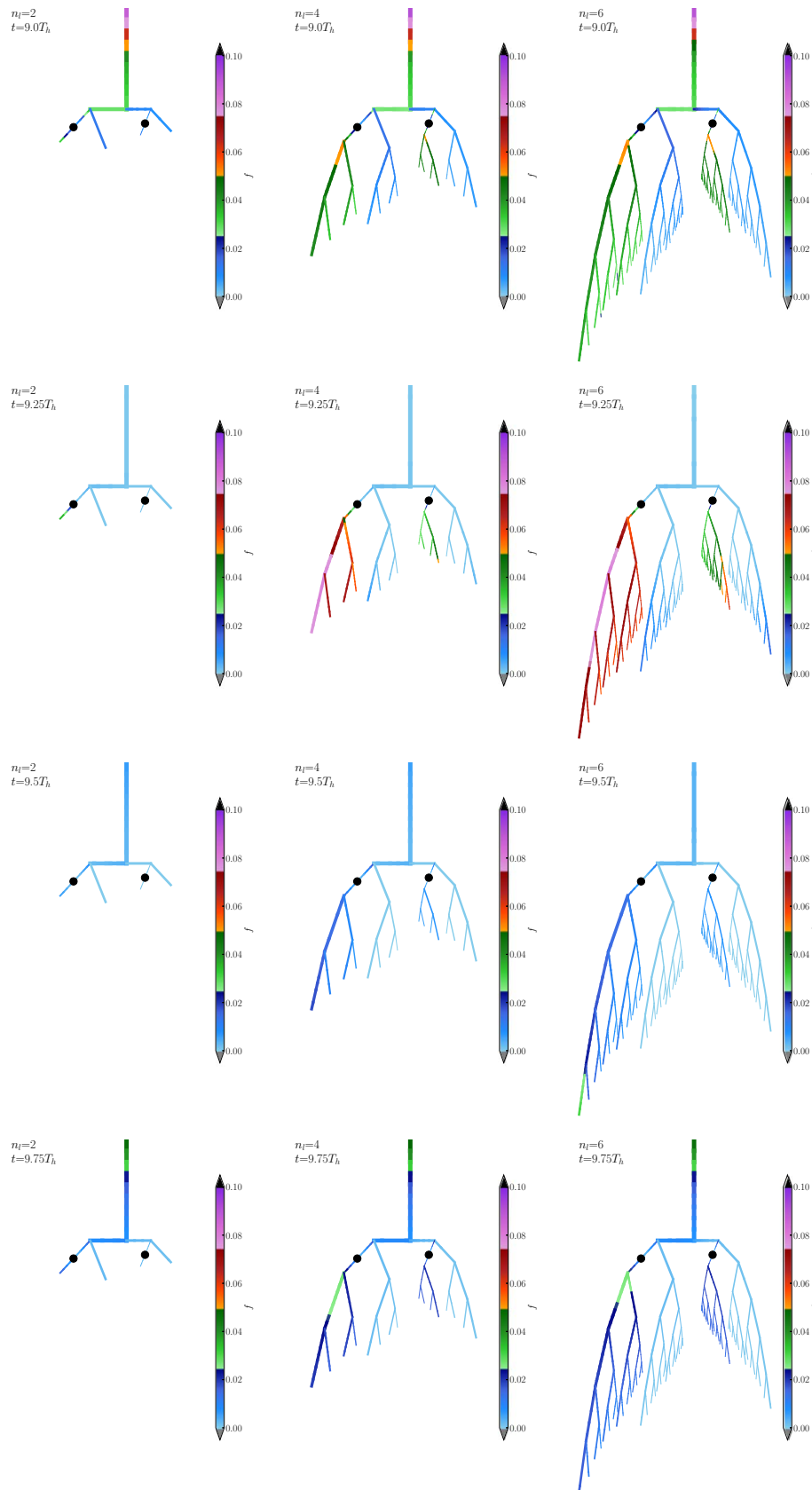


Fig. 10. Snapshots at $t_1 = 9T_h$, $t_2 = 9.25T_h$, $t_3 = 9.5T_h$ and $t_4 = 9.75T_h$ of the distribution of the structure parameter f in three networks with increasing levels of ramification $n_i \in \{2$ (left), 4 (middle), 6 (right) $\}$, presenting two stenosis marked by the black circles (O). Aggregation now occurs in the large arteries on the l.h.s of the network and in their immediate daughter arteries but also on the r.h.s, downstream of the stenosis. In the arteries upstream of the stenoses, aggregation is reduced due to the additional reflections created by the stenoses.

accurately compute network hemodynamics, especially in pathological networks.

7. Conclusion

We have proposed a time-dependent non-Newtonian extension of a 1D blood flow model, based on a classical 1D approach for the conservation mass and the balance of momentum, but including time- and structure-dependent viscous effects. The evolution of the shear stress is governed by a Maxwell equation with coefficients depending on the state of aggregation of RBCs. The balance between aggregation and shear-dependent disaggregation is described by a kinetic equation, which is a particular case of a structure model for viscoelastic fluids [14,18]. We note that this approach is not restricted to blood rheology and could be applied to other structured fluids.

We have confronted the numerical predictions of our 1D non-Newtonian blood flow model to experimental data available in the literature [17,73,74,77], and we have shown that the model reproduces qualitatively and quantitatively the rheology of blood. We have further investigated the non-Newtonian effects in arterial networks of increasing size and demonstrated how the pulsatility of the flow and the network topology contribute to the aggregation process, which occurs mainly in the large arteries and their immediate daughter arteries. The aggregation of RBCs is further increased downstream of pathologies such as stenoses.

In the entire study, we have assumed, in a 1D framework, that the WSR $\dot{\gamma}$ solely contributes to the disaggregation process as the structure of blood is represented by a single homogeneous phase. The WSR $\dot{\gamma}$ therefore governs the evolution of the blood structure near the wall and in the bulk of the flow. In reality, the axial velocity profile varies with time and space leading to variations of $\dot{\gamma}$ along the radius of the artery. In particular, for axisymmetric flow, $\dot{\gamma}|_{r=0} = 0$. By using the wall shear rate $\dot{\gamma}|_{r=R}$ to govern the disaggregation process in the entire artery, we have overestimated the shearing effects and therefore underestimated the non-Newtonian effects. However, we have also assumed an *a priori* shape of the velocity profile, which is valid for experimental validation (see Section 4) but an approximation for network flows. In Sections 5 and 6, we have assumed a Poiseuille flow everywhere in the network, as is classically done in 1D applications, and therefore underestimated the value of $\dot{\gamma}$. To overcome those limitations due to the loss of the velocity profile in the 1D averaging process, we plan in future works to use the 2D multiring blood flow model developed in [56] to compute the axial velocity profile and introduce radial variations in the aggregation process.

Keeping in mind these limitations inherent to the 1D framework, the 1D non-Newtonian blood flow model presented here will be useful in the future to help understand the hemodynamics in healthy and pathological networks of the micro- and macro-circulation.

References

- [1] S. Sherwin, L. Formaggia, J. Peiro, V. Franke, Computational modelling of 1D blood flow with variable mechanical properties and its application to the simulation of wave propagation in the human arterial system, *Int. J. Numer. Methods Fluids* 43 (6-7) (2003) 673–700.
- [2] L. Formaggia, D. Lamponi, A. Quarteroni, One-dimensional models for blood flow in arteries, *J. Eng. Math.* 47 (3-4) (2003) 251–276.
- [3] P. Perdikaris, G. Karniadakis, Fractional-order viscoelasticity in one-dimensional blood flow models, *Ann. Biomed. Eng.* 42 (5) (2014) 1012–1023.
- [4] E. Marchandise, M. Willemet, V. Lacroix, A numerical hemodynamic tool for predictive vascular surgery, *Med. Eng. Phys.* 31 (1) (2009) 131–144.
- [5] C. Audebert, P. Bucur, M. Bekheit, E. Vibert, I. Vignon-Clementel, J.-F. Gerbeau, Kinetic scheme for arterial and venous blood flow, and application to partial hepatectomy modeling, *Comput. Methods Appl. Mech. Eng.* 314 (2017) 102–125.
- [6] A. Ghigo, S.A. Taam, X. Wang, P.-Y. Lagr e, J.-M. Fullana, A one-dimensional arterial network model for bypass graft assessment, *Med. Eng. Phys.*
- [7] P. Blanco, M. Pivello, S. Urquiza, R. Feij o, On the potentialities of 3D–1D coupled models in hemodynamics simulations, *J. Biomech.* 42 (7) (2009) 919–930.
- [8] I. Vignon-Clementel, A. Marsden, J. Feinstein, A primer on computational simulation in congenital heart disease for the clinician, *Progress Pediat. Cardiol.* 30 (1) (2010) 3–13.
- [9] S. Sankaran, M. Moghadam, A. Kahn, E. Tseng, J. Guccione, A. Marsden, Patient-specific multiscale modeling of blood flow for coronary artery bypass graft surgery, *Ann. Biomed. Eng.* 40 (10) (2012) 2228–2242.
- [10] F. Cuomo, S. Roccabianca, D. Dillon-Murphy, N. Xiao, J. Humphrey, C. Figueroa, Effects of age-associated regional changes in aortic stiffness on human hemodynamics revealed by computational modeling, *PLoS One* 12 (3) (2017) e0173177.
- [11] L. Formaggia, J.-F. Gerbeau, F. Nobile, A. Quarteroni, On the coupling of 3D and 1D Navier–Stokes equations for flow problems in compliant vessels, *Comput. Methods Appl. Mech. Eng.* 191 (6) (2001) 561–582.
- [12] P. Blanco, R. Feij o, S. Urquiza, A unified variational approach for coupling 3D–1D models and its blood flow applications, *Comput. Methods Appl. Mech. Eng.* 196 (41) (2007) 4391–4410.
- [13] L. Formaggia, A. Quarteroni, C. Vergara, On the physical consistency between three-dimensional and one-dimensional models in haemodynamics, *J. Comput. Phys.* 244 (2013) 97–112.
- [14] M. Cross, Rheology of non-Newtonian fluids: a new flow equation for pseudoplastic systems, *J. Colloid Sci.* 20 (5) (1965) 417–437.
- [15] G. Thurston, Viscoelasticity of human blood, *Biophys. J.* 12 (9) (1972) 1205–1217.
- [16] G. Thurston, Elastic effects in pulsatile blood flow, *Microvascul. Res.* 9 (2) (1975) 145–157.
- [17] M. Bureau, J. Healy, D. Bourgoin, M. Joly, Rheological hysteresis of blood at low shear rate, *Biorheology* 17 (1-2) (1980) 191.
- [18] D. Quemada, R. Droz, Blood viscoelasticity and thixotropy from stress formation and relaxation measurements: a unified model, *Biorheology* 20 (5) (1982) 635–651.
- [19] C. Verdier, Review article: rheological properties of living materials. from cells to tissues, *J. Theor. Med.* 5 (2) (2003) 67–91.
- [20] Y. Cho, K. Kensey, Effects of the non-Newtonian viscosity of blood on flows in a diseased arterial vessel. Part 1: steady flows, *Biorheology* 28 (3-4) (1991) 241–262.
- [21] F. Yilmaz, M. Gundogdu, et al., A critical review on blood flow in large arteries; relevance to blood rheology, viscosity models, and physiologic conditions, *Korea–Australia Rheol. J.* 20 (4) (2008) 197–211.
- [22] A. Apostolidis, A. Beris, Modeling of the blood rheology in steady-state shear flows, *J. Rheol.* 58 (3) (2014) 607–633.
- [23] J. Bernsdorf, D. Wang, Non-newtonian blood flow simulation in cerebral aneurysms, *Comput. Math. Appl.* 58 (5) (2009) 1024–1029.
- [24] F.-B. Tian, L. Zhu, P.-W. Fok, X.-Y. Lu, Simulation of a pulsatile non-newtonian flow past a stenosed 2D artery with atherosclerosis, *Comput. Biol. Med.* 43 (9) (2013) 1098–1113.
- [25] N. Nandakumar, K. Sahu, M. Anand, Pulsatile flow of a shear-thinning model for blood through a two-dimensional stenosed channel, *Eur. J. Mech.-B/Fluids* 49 (2015) 29–35.
- [26] M. Jahangiri, M. Saghafian, M. Sadeghi, Numerical simulation of non-Newtonian models effect on hemodynamic factors of pulsatile blood flow in elastic stenosed artery, *J. Mech. Sci. Technol.* 31 (2) (2017) 1003–1013.
- [27] A. Apostolidis, A. Moyer, A. Beris, Non-Newtonian effects in simulations of coronary arterial blood flow, *J. Non-Newtonian Fluid Mech.* 233 (2016) 155–165.
- [28] F. Gijzen, F. van De Vosse, J. Janssen, The influence of the non-Newtonian properties of blood on the flow in large arteries: steady flow in a carotid bifurcation model, *J. Biomech.* 32 (6) (1999) 601–608.
- [29] F. Gijzen, E. Allanic, F. van De Vosse, J. Janssen, The influence of the non-Newtonian properties of blood on the flow in large arteries: unsteady flow in a 90 curved tube, *J. Biomech.* 32 (7) (1999) 705–713.
- [30] J. Weddell, J. Kwack, P. Imoukhuede, A. Masud, Hemodynamic analysis in an idealized artery tree: differences in wall shear stress between Newtonian and non-Newtonian blood models, *PLoS One* 10 (4) (2015) e0124575.
- [31] B. Moreau, B. Mauroy, Murray’s law revisited: Qu emada’s fluid model and fractal trees, *J. Rheol.* 59 (6) (2015) 1419–1430.
- [32] F. De Vita, M. de Tullio, R. Verzico, Numerical simulation of the non-newtonian blood flow through a mechanical aortic valve, *Theor. Comput. Fluid Dyn.* 30 (1-2) (2016) 129–138.
- [33] R.B. Bird, Useful non-Newtonian models, *Annu. Rev. Fluid Mech.* 8 (1) (1976) 13–34.
- [34] R. Owens, A new microstructure-based constitutive model for human blood, *J. Non-Newtonian Fluid Mech.* 140 (1) (2006) 57–70.
- [35] M. Moyers-Gonzalez, R. Owens, J. Fang, A non-homogeneous constitutive model for human blood. Part I. Model derivation and steady flow, *J. Fluid Mech.* 617 (2008) 327–354.
- [36] K. Yezeswarapu, M. Kameneva, K. Rajagopal, J. Antaki, The flow of blood in tubes: theory and experiment, *Mech. Res. Commun.* 25 (3) (1998) 257–262.
- [37] K. Rajagopal, A. Srinivasa, A thermodynamic frame work for rate type fluid models, *J. Non-Newtonian Fluid Mech.* 88 (3) (2000) 207–227.
- [38] M. Anand, K. Rajagopal, A shear-thinning viscoelastic fluid model for describing the flow of blood, *Int. J. Cardiovasc. Med. Sci.* 4 (2) (2004) 59–68.
- [39] M. Anand, J. Kwack, A. Masud, A new generalized oldroyd-b model for blood flow in complex geometries, *Int. J. Eng. Sci.* 72 (2013) 78–88.
- [40] J. Fang, R. Owens, Numerical simulations of pulsatile blood flow using a new constitutive model, *Biorheology* 43 (5) (2006) 637–660.
- [41] A. Duarte, A. Miranda, P. Oliveira, Numerical and analytical modeling of unsteady viscoelastic flows: the start-up and pulsating test case problems, *J. Non-Newtonian Fluid Mech.* 154 (2) (2008) 153–169.
- [42] M. Moyers-Gonzalez, R. Owens, J. Fang, A non-homogeneous constitutive model for human blood. Part III. Oscillatory flow, *J. Non-Newtonian Fluid Mech.* 155 (3) (2008) 161–173.
- [43] T. Bodn ar, A. Sequeira, M. Prosi, On the shear-thinning and viscoelastic effects of blood flow under various flow rates, *Appl. Math. Comput.* 217 (11) (2011)

- 5055–5067.
- [44] P. Perdikaris, L. Grinberg, G. Karniadakis, An effective fractal-tree closure model for simulating blood flow in large arterial networks, *Ann. Biomed. Eng.* 43 (6) (2015) 1432–1442.
- [45] T. Sochi, The flow of power law fluids in elastic networks and porous media, *Comput. Methods Biomech. Biomed. Eng.* 19 (3) (2016) 324–329.
- [46] J. Oldroyd, On the formulation of rheological equations of state, *Proceedings of the Royal Society of London A: Mathematical, Physical and Engineering Sciences*, The Royal Society, vol. 200, (1950), pp. 523–541.
- [47] G. Jager, *Electrical Model of the Human Systemic Arterial Tree*, University of Utrecht, 1965, Ph.d. thesis.
- [48] N. Westerhof, *Analog Studies of Human Systemic Arterial Hemodynamics*, PA: University of Pennsylvania, Philadelphia, 1968, Ph.d. thesis.
- [49] X.-F. Wang, J.-M. Fullana, P.-Y. Lagrée, Verification and comparison of four numerical schemes for a 1D viscoelastic blood flow model, *Comput. Methods Biomech. Biomed. Eng.* 18 (15) (2015) 1704–1725.
- [50] A. Ghigo, X.-F. Wang, R. Armentano, J.-M. Fullana, P.-Y. Lagrée, Linear and non-linear viscoelastic arterial wall models: application on animals, *J. Biomech. Eng.* 139 (1) (2017) 011003.
- [51] P.-Y. Lagrée, S. Lorthois, The RNS/Prandtl equations and their link with other asymptotic descriptions: application to the wall shear stress scaling in a constricted pipe, *Int. J. Eng. Sci.* 43 (3) (2005) 352–378.
- [52] F. Smith, Flow through constricted or dilated pipes and channels: Part 2, *Q. J. Mech. Appl. Math.* 29 (3) (1976) 365–376.
- [53] J. Womersley XXIV, Oscillatory motion of a viscous liquid in a thin-walled elastic tube. I: the linear approximation for long waves, *London, Edinburgh, Dublin Philosoph. Mag. J. Sci.* 46 (373) (1955) 199–221.
- [54] S. Suter, R. Skalak, The history of Poiseuille's law, *Annu. Rev. Fluid Mech.* 25 (1) (1993) 1–20.
- [55] Y. Fung, *Biomechanics: Circulation*, Springer Science & Business Media, 2013.
- [56] A. Ghigo, J.-M. Fullana, P.-Y. Lagrée, A 2D nonlinear multiring model for blood flow in large elastic arteries, *J. Comput. Phys.* 350 (2017) 136–165.
- [57] J. Rosenblatt, *The Rheology of Blood: A Structured Fluid Approach Based on Rouleau Behaviour*, University of California, Berkeley, 1988, Ph.d. thesis.
- [58] R. Carr, M. Lacoïn, Nonlinear dynamics of microvascular blood flow, *Ann. Biomed. Eng.* 28 (6) (2000) 641–652.
- [59] J. Geddes, R. Carr, N. Karst, F. Wu, The onset of oscillations in microvascular blood flow, *SIAM J. Appl. Dyn. Syst.* 6 (4) (2007) 694–727.
- [60] J. Mewis, N. Wagner, *Colloidal Suspension Rheology*, Cambridge University Press, 2012.
- [61] A. Apostolidis, M. Armstrong, A. Beris, Modeling of human blood rheology in transient shear flows, *J. Rheol.* 59 (1) (2015) 275–298.
- [62] R. Owens, T. Phillips, *Computational Rheology*, World Scientific, 2002.
- [63] T. Hughes, J. Lubliner, On the one-dimensional theory of blood flow in the larger vessels, *Math. Biosci.* 18 (1) (1973) 161–170.
- [64] Y. Ikenaga, S. Nishi, Y. Komagata, M. Saito, P.-Y. Lagree, T. Asada, M. Matsukawa, Experimental study on the pressure and pulse wave propagation in viscoelastic vessel tubes – effects of liquid viscosity and tube stiffness, *IEEE Trans. Ultrason. Ferroelect. Frequency Control* 60 (11) (2013) 2381–2388.
- [65] X.-F. Wang, S. Nishi, M. Matsukawa, A. Ghigo, P.-Y. Lagrée, J.-M. Fullana, Fluid friction and wall viscosity of the 1D blood flow model, *J. Biomech.* 49 (4) (2016) 565–571.
- [66] C. Puelz, S. Čanić, B. Rivière, C. Rusin, Comparison of reduced models for blood flow using Runge–Kutta discontinuous Galerkin methods, *Appl. Numer. Math.*
- [67] P.-Y. Lagrée, An inverse technique to deduce the elasticity of a large artery, *Eur. Phys. J. Appl. Phys.* 9 (02) (2000) 153–163.
- [68] N. Smith, A. Pullan, P. Hunter, An anatomically based model of transient coronary blood flow in the heart, *SIAM J. Appl. Math.* 62 (3) (2002) 990–1018.
- [69] A. Ghigo, O. Delestre, J.-M. Fullana, P.-Y. Lagrée, Low-Shapiro hydrostatic reconstruction technique for blood flow simulation in large arteries with varying geometrical and mechanical properties, *J. Comput. Phys.* 331 (2017) 108–136.
- [70] F. Bouchut, *Nonlinear Stability of Finite Volume Methods for Hyperbolic Conservation Laws and Well-Balanced Schemes for Sources*, Springer Science & Business Media, 2004.
- [71] J. Murillo, P. García-Navarro, A Roe type energy balanced solver for 1D arterial blood flow and transport, *Comput. Fluids* 117 (2015) 149–167.
- [72] H. Steffan, W. Brandstätter, G. Bachler, R. Pucher, Comparison of newtonian and non-newtonian blood flow in stenotic vessels using numerical simulation, *Biofluid Mechanics*, Springer, 1990, pp. 479–485.
- [73] J. Barbee, *The Flow of Human Blood Through Capillary Tubes with Inside Diameters Between 8.7 and 221 Microns*, California Institute of Technology, 1971, Ph.d. thesis.
- [74] D. McMillan, J. Strigberger, N. Utterback, Rapidly recovered transient flow resistance: a newly discovered property of blood, *Am. J. Physiol.-Heart Circul. Physiol.* 253 (4) (1987) H919–H926.
- [75] J. Barbee, G. Cokelet, Prediction of blood flow in tubes with diameters as small as 29 μ , *Microvascul. Res.* 3 (1) (1971) 17–21.
- [76] E. Merrill, G. Cokelet, A. Britten, R. Wells, Non-newtonian rheology of human blood-effect of fibrinogen deduced by "subtraction", *Circul. Res.* 13 (1) (1963) 48–55.
- [77] M. Bureau, J. Healy, D. Bourgoin, M. Joly, Etude rhéologique en régime transitoire de quelques échantillons de sangs humains artificiellement modifiés, *Rheol. Acta* 18 (6) (1979) 756–768.
- [78] M. Olufsen, Structured tree outflow condition for blood flow in larger systemic arteries, *Am. J. Physiol.-Heart Circul. Physiol.* 276 (1) (1999) H257–H268.
- [79] M. Olufsen, C. Peskin, W. Kim, E. Pedersen, A. Nadim, J. Larsen, Numerical simulation and experimental validation of blood flow in arteries with structured-tree outflow conditions, *Ann. Biomed. Eng.* 28 (11) (2000) 1281–1299.
- [80] P. Blanco, S. Watanabe, E. Dari, M. Passos, R. Feijóo, Blood flow distribution in an anatomically detailed arterial network model: criteria and algorithms, *Biomech. Model. Mechanobiol.* 13 (6) (2014) 1303–1330.
- [81] Y. Fan, W. Jiang, Y. Zou, J. Li, J. Chen, X. Deng, Numerical simulation of pulsatile non-Newtonian flow in the carotid artery bifurcation, *Acta Mechanica Sinica* 25 (2) (2009) 249–255.